Springer

Acta Mechanica Sinica

CrossMark click for updates

• RESEARCH PAPER •

Acta Mech. Sin., Vol. 40, 323621 (2024)
https://doi.org/10.1007/s10409-024-23621-x

Hybrid approach for simulating flow-induced sound around moving bodies based on ghost-cell immersed boundary method

Cheng Zhao[1], Hong-Gang Li[1], Xue-Gang Li[1], Yan Yang[2,3*], and Kai Cui[2,3]

[1] *Wuhan Second Ship Design and Research Institute, Wuhan 430205, China;*
[2] *LHD, Institute of Mechanics, Chinese Academy of Sciences, Beijing 100190, China;*
[3] *School of Engineering Sciences, University of Chinese Academy of Sciences, Beijing 100049, China*

Received December 16, 2023; accepted January 28, 2024; published online July 22, 2024

A hybrid approach based on the immersed boundary method (IBM) is developed for computation of flow-induced sound around moving bodies. In this method, a high-fidelity direct numerical simulation (DNS) solver is used to simulate the incompressible flow field. The sound field is predicted by discretizing acoustic perturbation equations (APEs) with dispersion-relation-preserving space scheme and low-dispersion and low-dissipation Runge-Kutta time integration. A sharp-interface IBM based on ghost-cell is implemented for present two-step DNS-APE approach to deal with complex moving bodies with Cartesian grids. The present method is validated through simulations of sound generation caused by flow past a rotating cylinder, an oscillating cylinder, and tandem oscillating and stationary cylinders. The sound generated by typical kinds of complicated bio-inspired locomotions, i.e., flapping flight by wings of varied shapes and collective undulatory swimming in tandem, are investigated using present method. The results demonstrate potential of the hybrid approach in addressing flow-induced sound generation and propagation with complex moving boundaries in a fluid medium, especially for the sound characteristics of bio-mimetic flows, which might shed lights on investigations on bio-acoustics, ethology of complex animal system, and related bio-mimetic design for quietness.

Flow-induced sound, Immersed boundary method, Moving boundary, Bio-inspired locomotion, Computational aero/hydro-acoustics

Citation: C. Zhao, H.-G. Li, X.-G. Li, Y. Yang, and K. Cui, Hybrid approach for simulating flow-induced sound around moving bodies based on ghost-cell immersed boundary method, Acta Mech. Sin. 40, 323621 (2024), https://doi.org/10.1007/s10409-024-23621-x

1. Introduction

Prediction of flow-induced sound and noise reduction are important for the performance of many engineering systems, such as underwater vehicle, aircraft, and turbomachine. Recently, the requirement to reduce and control the radiated noise generated by these structures and devices is increasing. The aquatic and aerial animals in nature present excellent locomotion performances, including high efficiency, low noise, and long endurance ability [1,2]. Thus, investigations on sound generation mechanism and propagation characteristics of bio-inspired locomotions are crucial for the design of quietness or acoustic-invisibility of man-made vehicles, such as micro air vehicles and unmanned underwater vehicles [3]. Besides, sound generated by bio-inspired locomotion may be used to release sound signals for communication, sex, and reproduction and could affect fishes' lives and behaviors [4-6].

In previous studies, three categories of computational aeroacoustics (CAAs) methods were proposed to investigate flow-induced sound problems, including direct noise computation (DNC), acoustic analogy method, and hydrodynamic/acoustic splitting approach [7]. The DNC discretizes the compressible Navier-Stokes (NS) equations directly and obtains the flow performance as well as the sound field simultaneously. The sound generation and wave propagation can be described without any limitations and

*Corresponding author. E-mail address: yangyan@imech.ac.cn (Yan Yang)
Executive Editor: Lihao Zhao

assumptions. However, this method requires a fine grid and the computational cost is very high for most practical problems as both of the scales of small turbulence eddies and high frequency sound waves should be depicted simultaneously and a reasonable long computational time should be simulated. For the acoustic analogy method, the unsteady flow, representing the sound sources by specific models, are firstly obtained by various numerical methods, i.e., computational fluid dynamics (CFDs) techniques, including finite difference method, finite element method, and finite volume method. Then the radiated sound is solved by the acoustic analogy equation/models. These analogy methods include Lighthill's analogy and Curle's equation, FW-H equations and Kirchhoff methods, etc. The acoustic analogy methods described the sound propagation in a stationary or uniform flow and the effect of non-uniform flow or non-compact sound sources on the sound field cannot be solved because of the strict theoretical requirements [7,8]. Another hybrid approach called the hydrodynamic/acoustic splitting approach, which was first derived by Hardin and Pope [9], and was developed by Shen et al. [10,11]. This method can describe the sound propagation in the non-uniform flow and is considered to be an effective method for simulating sound fields generated by low-Mach-number, non-compact source. A similar concept was proposed for deriving acoustic perturbation equations (APEs) [12] and linearized perturbed compressible equations [13], where only the acoustic mode is considered and the hydrodynamic instabilities and perturbed vorticity are prevented, which is different from the linear Euler equations who does not distinguish varied perturbations in the flow.

Although the CAA methods have been developed rapidly, it is challenging for the simulation of flow-induced sound problems with complex moving bodies, especially large displacement and large deformation problems. The high-quality grid generation is usually difficult and the re-meshing procedure is also high cost for these problems. The immersed boundary method (IBM) [14] is an effective method to simulate complex geometries and moving boundaries. Compared with the traditional body-fitted grid, the fixed Cartesian grid system is used to discretize the governing equations and the grid generation progress is greatly simplified for very complex geometry and moving boundary problems, such as bio-inspired flow problems [15]. In recent years, the IBM was used to study acoustic propagation and flow-induced sound problems. Komatsu et al. [16] and Hattori and Komatsu [17] used the corrected volume penalization IBM to predict the aeroacoustic problems by the compressible direct numerical simulation (DNS) method. Wang et al. [18] presented a diffusion-interface penalty IBM for simulating fluid-structure-acoustics interactions with large deformation boundaries. Cheng et al. [19] implemented a semi-implicit body-force based IBM in the compressible NS equations and utilized a prediction-correction technique for simulating the sound generated by moving bodies. In these methods, the solid boundary treatments were satisfied within a localized region and the approximate delta function leads to local first-order accuracy near the solid boundary. Besides, the DNS requires high computational costs and it is difficult to simulate high Reynolds number problems. Another ghost-cell (GC) based IBM can keep the sharp-interface quality via interpolation near wall boundaries. Seo and Mittal [20] proposed a high-order sharp-interface IBM to predict the flow-induced sound around complex moving bodies. The high-order polynomial interpolation may reduce the interpolation efficiency and lead to numerical instabilities when most of the interpolation stencils used for the GC are solid points themselves. Xie et al. [21] proposed a sharp-interface IBM to simulate sound scattered by arbitrarily complex geometries and results show the method can achieve a second-order accuracy. He et al. [22] used a wavelet IBM for simulating fluid-structure-sound interactions with elastic boundaries and studied the effect of boundary stiffness on sound field. However, the oscillating motion and large deformation boundaries are not considered. In Ref. [23], a GC based IBM for simulating flow-induced sound problems with complex geometry is proposed and the flow-induced sound of flow past a four-cylinder array was investigated as an application of the method.

In this study, a hybrid approach based on the IBM is proposed to predict the sound generation by moving bodies in the fluid medium. The unsteady incompressible flow is used to obtain the sound source by the DNS solver, as previous work did. The second step is to predict the acoustic propagation in a time-averaged non-uniform flow by solving APE, with the source terms and flow quantities gained from the CFD solver. The sharp-interface IBM is enforced on the moving body and the GCs is proposed to satisfy the various solid boundary conditions, both in the CFD part and the APE part, i.e., for the flow field and for the sound field. The hybrid approach has the characteristics of high accuracy and simulates time-dependent acoustic field explicitly for the flow-induced sound by moving bodies, suitable for aero and hydro-acoustic problems. Flow-induced sound generation and sound propagation characteristics of flapping flight and undulatory swimming are both demonstrated, the relevant features of which may inspire the marine biology and biomimetics of flying and swimming.

The paper is organized as follows: Sect. 2 describes the governing equations of the hybrid approach of CAAs and the numerical methodology. In Sect. 3, sound generation by a rotating cylinder, an oscillating cylinder, and oscillating and stationary cylinders in tandem were used to validate the hybrid method. The sound generated by typical complicated bio-inspired locomotions, i.e., the flapping wings and the undulating foils in tandem, are further investigated to de-

monstrate the versatility of the method for large displacement and large deformation problems. Finally, conclusions are presented in Sect. 4.

2. Numerical method

2.1 Incompressible flow field

The flow field are described by following incompressible viscous Navier-Stokes (INS) equations:

$$\nabla \cdot \mathbf{U} = 0, \tag{1}$$

$$\frac{\partial \mathbf{U}}{\partial t} + (\mathbf{U} \cdot \nabla)\mathbf{U} = -\frac{1}{\rho_0}\nabla P + v_0 \nabla^2 \mathbf{U}, \tag{2}$$

where ρ_0 and v_0 are the fluid density and kinematic viscosity, respectively; $\mathbf{U}$ is the velocity vector; P is the pressure; t is the time.

The second-order central difference scheme is used to discretize the INS equations in space on a cell-centered, collocated grid system using the primitive variables of velocity and pressure. The fractional step method involving three sub-steps with second-order accuracy was used for time-integration. In the first sub-step, the convection term is discretized by the Adams-Bashforth scheme and the diffusion term is discretized by the implicit Crank-Nicolson scheme. Then the intermediate velocity can be computed. In the next sub-step, the pressure correction Poisson equation is solved to obtain the pressure correction value, which is used to update the pressure and velocity in the last sub-step. As presented in Ref. [24], this collocated scheme has a simpler implementation than a conventional fully staggered scheme, where only the face velocity component normal to the cell-face is calculated and used for computing the volume flux from each cell. The face-velocities are used in estimating the convective term in the first sub-step, and are separately updated in the third sub-step, which satisfies discrete mass-conservation and decreases the possibility of producing oscillatory pressure or velocity fields.

For the computational domain boundary, a uniform incoming velocity is applied at the inlet and lateral boundaries. At the outlet boundary, an outflow boundary condition is used to eliminate the boundary reflections. The homogeneous Neumann boundary condition is applied to the pressure boundaries. This incompressible CFD solver was validated by canonical flow problems and has been proven to be successful in simulating complex moving boundary problems such as bio-inspired flow problems [24].

2.2 Sound field

The sound wave propagation in a non-uniform flow is described by APEs [12]. The total primitive variables were split into a mean term and a fluctuating term, and two parts were inserted into the compressible NS equations. By discarding the non-linear terms and assuming that the sound perturbation velocity is irrotational, several governing equations and source terms were derived. For the low-Mach number vortex sound sources, the APE can be expressed as [12]

$$\frac{\partial p'}{\partial t} + \bar{c}_0{}^2 \nabla \cdot \left(\bar{\rho}_0 \mathbf{u'} + \overline{\mathbf{U}} \frac{p'}{\bar{c}_0{}^2} \right) = 0, \tag{3}$$

$$\frac{\partial \mathbf{u}'}{\partial t} + \nabla (\overline{\mathbf{U}} \cdot \mathbf{u'}) + \nabla \left(\frac{p'}{\bar{\rho}_0} \right) = \frac{\nabla P'}{\rho_0}, \tag{4}$$

where p' is the sound pressure, $\mathbf{u'}$ is the irrotational perturbation velocity; and c_0 is the sound speed. The time-averaged terms are denoted by a bar symbol, which is computed when the steady-state is achieved. The sound propagation considering the convection and refraction effects can be described in the APE and the vortex sound sources are expressed on the right-hand side. Here, p' (= $P - \overline{P}$) denotes the pressure fluctuation and ∇ is the gradient operator. In this APE system, only acoustic modes are excited and the sound generated by vorticity mode and entropy mode are not considered, thus the hydrodynamic instabilities is prevented for arbitrary mean flow field [12].

Compared with the traditional CFD schemes, the numerical schemes for acoustic simulation require minimal numerical dispersion and dissipation properties, which can be accomplished by using optimized high-order finite difference schemes. In the present study, the 4th-order dispersion-relation-preserving (DRP) scheme using 7-point stencil [25] is adopted and the first derivative for symmetrically central stencils can be written as

$$\frac{\partial f}{\partial x}(x_0) = \frac{1}{\Delta x} \sum_{j=-3}^{3} a_j f(x_0 + j\Delta x), \tag{5}$$

where a_j is the constant coefficient given as [25]

$$a_0 = 0,$$
$$a_1 = -a_{-1} = 0.77088238051822,$$
$$a_2 = -a_{-2} = -0.16670590441458,$$
$$a_3 = -a_{-3} = 0.02084314277031.$$

The unsymmetrical backward stencils [26] are applied near the computational domain boundaries. Near the solid boundaries, stencils with smaller size are applied to keep the numerical stability. Specifically, the sizes of the stencils are decreased to 3 and 5 points at the first and second fluid cells near the solid boundary and the spatial accuracy are of order 2 and 4, respectively. The stretching grids are used in the present method and fine grid points are generated near the solid boundary.

The low-dissipation and low-dispersion Runge-Kutta (LDDRK) scheme [27] is performed for time integration to minimize the dissipation and dispersion errors. From the nth time step to the $(n + 1)$th time step, the LDDRK iteration

was divided into 6 stages explicitly, which can be expressed as follows:

$$\mathbf{U}^{n+1} = \mathbf{U}^n + \sum_{i=1}^{6} w_i K_i, \tag{6}$$

$$K_i = \Delta t F\left(\mathbf{U}^n + \sum_{j=1}^{i-1} \beta_{ij} K_j\right), \ i = 1, 2, ..., 6, \tag{7}$$

where vector $\mathbf{U}$ represents the values at the grid points and the F contains the spatial discretization. w_i and β_{ij} are constant coefficients [27] and Δt is the acoustic time step.

To suppress the numerical oscillations and keep the numerical stability, the high-order spatial filtering [28] is applied. The 10th-order accuracy using 11-point stencils is implemented in the present method and the number of the stencil point is also reduced at the boundary. The acoustic radiation boundary conditions [29] are applied in the computational domain boundaries for the sound wave absorption.

2.3 Solution procedures

The acoustic solver and fluid solver are separated, so that for different flow regimes, the corresponding flow solver could be implemented and combined with the high-accuracy acoustic solver expediently, which adds versatility to the present flow-acoustic coupled solver, i.e., the hybrid CAA method. The solution procedures of the present DNS-APE hybrid approach for flow-induced sound problems are presented in Fig. 1. After generating the computational grid and initializing the flow field, second-order discretization is applied to solve INS equations. The mean flow field and sound source at each flow time step input into the acoustic solver when the flow field converged. The high-order numerical scheme is used to discretize the APE and the sound field can be obtained at each time step.

2.4 IBM for moving boundaries

For the present IBM applied in the above two steps, i.e., the CFD flow solver and the APE acoustic solver, the flow field is solved on the fixed Eulerian grid system, and the solid surface and moving boundary are represented by the Lagrangian grid system. The computational domains and grids of the flow field and the acoustic field are the same for present cases to eliminate the numerical effects of interpolation between the flow and acoustic simulation. However, the two grid systems can also be different to reduce the computational cost and it is necessary to conduct the spatial interpolation under this condition. For the boundary treatment, the IBM based on the GC is implemented in the present method and the advantage of the present IBM is that the sharpness of the boundary interface can be kept. This approach of IBM is under the category of the known "discrete forcing" approach, distinguished from the "continuous forcing" approach. The boundary condition on the IB is imposed by use of GCs. The method involves the calculation of variables on GCs inside the solid body, ensuring that the boundary conditions are precisely satisfied on the immersed boundary. This leads to a "sharp" representation of the immersed boundary without the need for ad-hoc constants or momentum forcing terms [24].

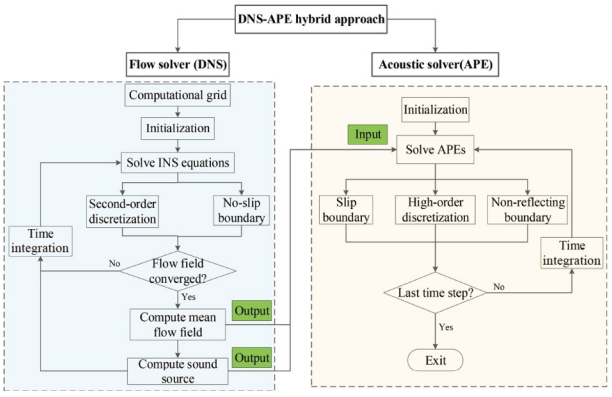

Figure 1 Schematic of the solution procedure for DNS-APE hybrid approach.

The schematic of the computational grid near a serrated geometry body is presented in Fig. 2(a). The Cartesian cell was classified into three parts according to the position between the cell and the solid boundary. For the external flow problem, the cell outside the solid boundary is a fluid cell and the inner cell is a solid cell. The GC, which is used as the finite difference stencil near the solid boundary, is located in the solid domain and has at least one neighboring fluid cell, as shown in Fig. 2(b). As a second-order central difference scheme with a 3-point stencil is applied near the solid boundary in the present method, only one layer of GC inside the solid boundary is considered and the interpolation procedure can be simplified significantly. In order to obtain the variables on the GC, a perpendicular line starting from the GC extends to the boundary-intercept (BI) point on the surface of the solid. This line segment is continuously extended from the BI point to a special point called image point (IP) and the distance between the IP and BI is the same as the distance between the BI and GC, as shown in Fig. 2(b) [24]. The variables φ around the IP can be interpolated by the surrounding cells. Here, a bilinear interpolation (tri-linear interpolation for 3D problems) is applied to compute the variables on the IP.

For the above procedure, if all the cells surrounding the IP are fluid cells, such as point IP1 in Fig. 2(b), the interpolation can be implemented directly. If the cell surrounding the IP is the GC itself, such as IP2, the values on the IP2 are coupled to the variables on the GC and coupled equations are solved. Once interpolated variable values at the IP are obtained, the linear extrapolation is conducted to compute the variables on the GC based on the boundary conditions.

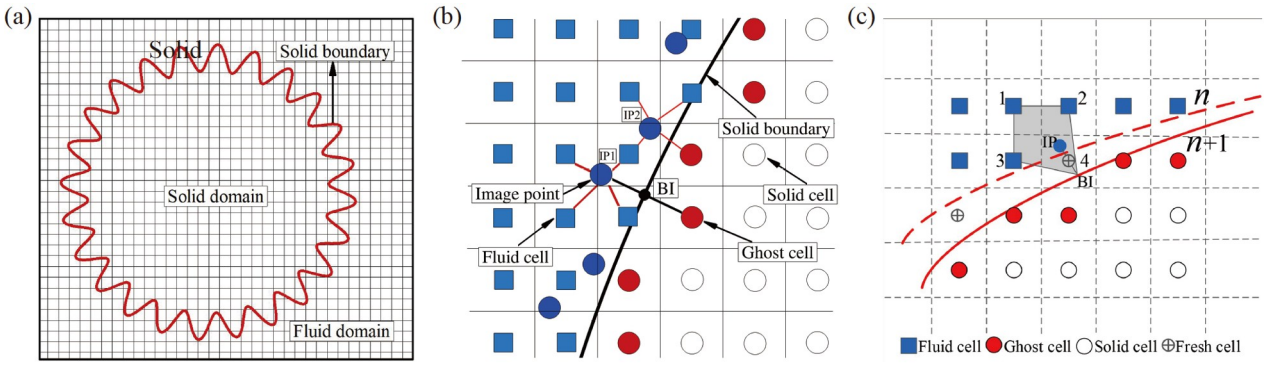

Figure 2 (a) Schematic of the computational grid near the solid body. (b) Immersed boundary treatment near the solid body. (c) IBM for moving case.

For the flow field and acoustic field, the no-slip boundary condition and slip boundary condition are satisfied, respectively.

$$\frac{\partial P}{\partial n} = 0,\ \mathbf{U} = \mathbf{U}_s, \tag{8}$$

$$\frac{\partial p'}{\partial n} = 0,\ \mathbf{u}' \cdot \mathbf{n} = 0, \tag{9}$$

where vector **n** represents the normal direction of the solid wall; $\mathbf{U}_s$ is the motion velocity of the solid boundary. For the Dirichlet boundary and Neumann boundary, the expressions can be described as

$$\varphi_{\mathrm{GC}} = 2\varphi_{\mathrm{BI}} - \varphi_{\mathrm{IP}}, \tag{10}$$

$$\varphi_{\mathrm{GC}} = \varphi_{\mathrm{IP}} + \Delta l\left(\frac{\delta\varphi}{\delta n}\right)_{\mathrm{BI}}, \tag{11}$$

where subscript GC, BI, and IP denote the variables on the GC, boundary intercept point and IP, respectively. Δl represents the distance between the GP and IP.

For the moving boundary treatment, the above procedures need to be conducted at every time step. The Lagrangian point of the solid surface is first moved to the new location. If the motion or the deformation of the body is a known function (prescribed motion), the motion can be predicted directly. If the flow is coupled to the structure (fluid-structure interaction), the dynamical equation of the solid is used to predict the motion. Next, the solid boundary treatment is similar to the stationary case. For the present GC based sharp interface IBM, the "fresh-cell" problem [24] can be encountered for moving boundary problems. That is, a cell inside the solid body (solid cell or GC) at the local time step suddenly becomes the fluid cell at the next time step due to body motion/deformation, as shown in Fig. 2(c). As the variables on the fresh cell have no time histories, the unknown variables on the fresh-cell are interpolated by surrounding fluid cells. Similar to the IBM treatment for stationary case, a perpendicular line starting from the fresh-cell extends to the "BI" point at the current step ($n+1$ step). The geometric location of the fresh cell is in the middle of IP and BI. A bilinear interpolation for the fresh-cell values is performed by using the four cells of the quadrilateral region, as shown in Fig. 2(c).

3. Results and discussion

3.1 Sound generated by flow past a rotating cylinder

References [23,30,31] have presented a series of validation cases for acoustic propagation, scattering, and flow-induced sound with stationary bodies, which demonstrated the high-accuracy and minimal dissipation and dispersion of the acoustic solver and the feasibility of the method for simulating flow-induced sound around complex stationary bodies. Note that, for the radiation problems with analytic solutions without boundary, the spatial 4-th order accuracy has been achieved, which is close to the ideal accuracy of the spatial scheme, 4-th order DRP. For the problem with immersed solid boundary, the spatial accuracy drops down to about 2.3, because of the boundary treatment. In this work, cases are all for moving boundaries to validate the capability and accuracy of the current method.

Firstly, the flow-induced sound generated by a rotating cylinder is computed. The cylinder with diameter D performs rotary motion around the center O in an anticlockwise direction, as shown in Fig. 3. The x-axis and y-axis are parallel and normal to the incoming flow direction, respectively. The polar coordinate system (r, θ) is also defined for directivity pattern. The incoming flow velocity is U_0 and the rotary velocity $U_\theta = 1.5U_0$ [18,32]. The Reynolds number $Re = U_0D/\nu_0 = 160$, Mach number $Ma = U_0/c_0 = 0.2$.

For the present case, the computational Cartesian grid of the flow field is the same as the acoustic field and a dense boundary layer grid is applied near the cylinder. Since flow simulation requires a much finer grid in order to capture the boundary layer, grid independence studies are performed by comparing the time histories of drag coefficient (C_{D}) and lift coefficient (C_{L}) on three different grids, i.e., the coarse ($\Delta x_{\min} = \Delta y_{\min} = 0.025D$), medium ($\Delta x_{\min} = \Delta y_{\min} = 0.015D$) and fine ($\Delta x_{\min} = \Delta y_{\min} = 0.01D$) grids. The time histories of C_{D} and C_{L} are presented in Fig. 4. The amplitude differences

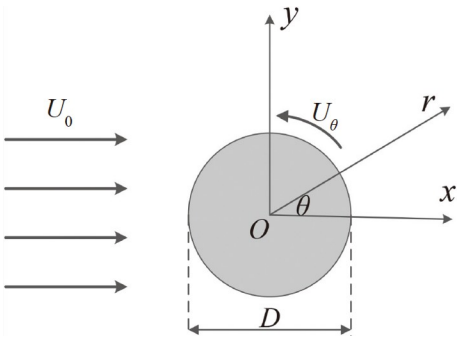

Figure 3 Schematic of flow past a rotating cylinder.

of the C_D and C_L for medium grid and fine grid are less than 1.5%, which demonstrates that the results were grid-independent. In order to resolve the far-field sound waves, the maximum grid size is $1.3L$ and the uniform grid is applied. The computational domain is $0 \le (x, y) \le 200D$ and the total numbers of grids for a medium grid system is 512 × 512. Compared to the classical flow over a circular cylinder, as shown in Figs. 12 and 13 in Ref. [23], it is observed that the symmetry of C_L is broken and a large lift coefficient (mean value is about −3.5) is obtained with amplitude nearly unchanged. Moreover, the mean C_D decreases remarkably with a larger amplitude. These lead to a large lateral resultant fluid force, as could be explained by the Magnus effect.

The instantaneous sound field and the magnitudes of the sound pressure along $x = 100D$ line (dash line in the contour) at two instants are presented in Fig. 5(a) and (b). A spiral sound field is observed due to the rotary motion of the cylinder, which is different from the dipolar sound source generated by the stationary cylinder. The perturbations with a short wave length in the near wake region might be regarded as pseudo-sound or small scale eddies generated due to the transitional wake [33]. The pseudo-sound dissipates much faster and is not presented in the far field. The magnitudes of the sound pressure along $x = 100D$ line decrease with increasing distance. The sound pressure above the cylinder at every instant is slightly larger than that below the cylinder due to the anticlockwise rotation. The peak values of sound pressure measured at $\theta = 90°$ were extracted along the radial coordinate in Fig. 5(c). The decay rate of sound pressure peaks is similar to the results of the stationary cylinder, which is proportion to $r^{-1/2}$ (the blue dashed line). The directivity patterns at $r = 75D$ are presented in Fig. 5(d), it shows that the pattern is not symmetric any longer due to the rotation and the magnitude of sound pressure is also higher than that of the stationary cylinder, probably related to the Magnus effect as well. The present result has a slight quantitative difference between the present and the previous two DNS results [18,32], with good agreement of qualitative characteristics, which demonstrates the accuracy of the hybrid method dealing with a moving boundary. Besides, there are slight quantitative differences, especially at around 80

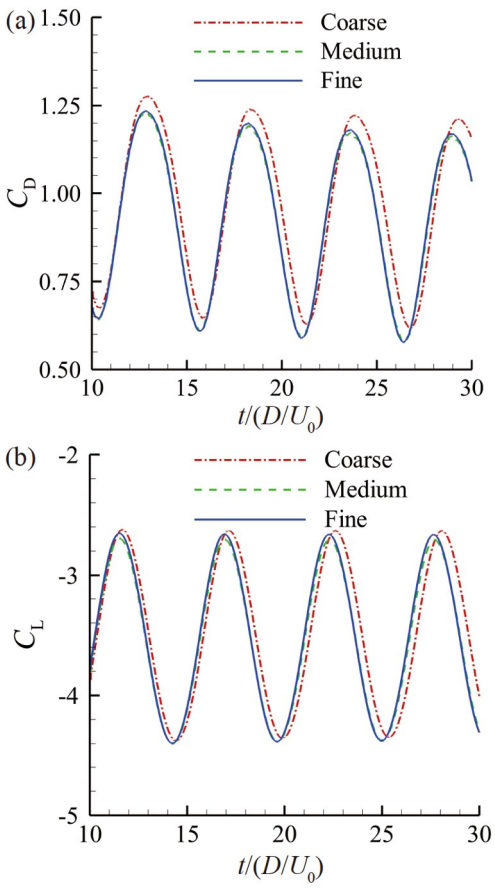

Figure 4 Grid independence test of the (a) drag coefficient and (b) lift coefficient of the rotating cylinder.

degree direction, which could be caused by differences in schemes, coding, or the numerical filtering they implemented.

3.2 Sound generated by flow past an oscillating cylinder

In this problem, the sound generation by an oscillating cylinder (as shown in Fig. 6) is simulated to validate the present method for large displacement problems. The incoming flow velocity is U_0. A cylinder with diameter D is located at the center of the computational domain at $t = 0$ and the oscillating motion is prescribed as $y(t) = A\sin(2\pi t \times f)$, where $A = 0.2D$ is the amplitude and f is the frequency. Two cases with $f = 0.15$ and $f = 0.22$ are considered, which are lower and higher than the vortex shedding frequency (≈ 0.18) of the stationary cylinder. The $Re = 150$ and $Ma = 0.2$. The computational domain size is $0 \le (x, y) \le 200D$ and a non-uniform 512 × 512 Cartesian grid with minimum grid $dx = dy = 0.01D$ is applied around the oscillating cylinder.

The instantaneous vorticity ω at $y = 0$ for two cases are presented in Fig. 7. The wake structures of two oscillating frequencies are significantly different. When $f = 0.15$, the periodic vortex street is observed, which is similar to the

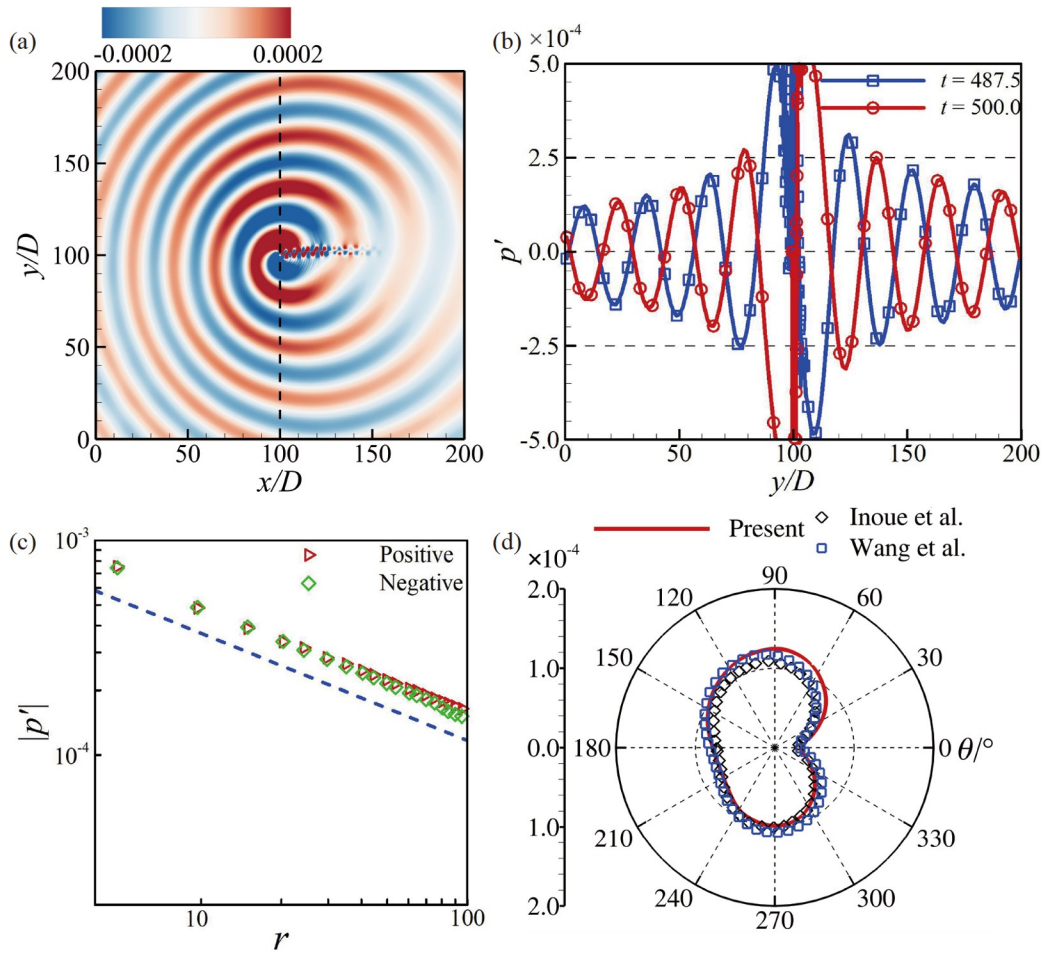

Figure 5 (a) Instantaneous sound field and (b) the magnitudes of the pressure along $x = 100D$ line. (c) Peak values of the sound pressure against distance r at $\theta = 90°$ direction. (d) Directivity patterns at $75D$.

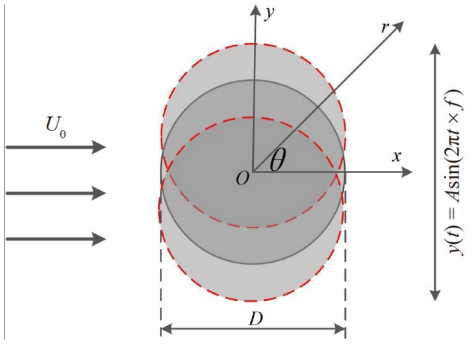

Figure 6 Computational modeling of flow past an oscillating circular cylinder.

result of the stationary cylinder. However, the distance between adjacent vortices is different and the flow field is not periodic at $f = 0.22$. The vortex generates at $x \leq 105D$ and evolves into a shear layer at $105D \leq x \leq 110D$. Subsequently, a compact vortex occurs at $x \geq 110D$. The present vortex structures are similar to Refs. [16,17], which demonstrates the effectiveness of the present flow solver for large deformation problems.

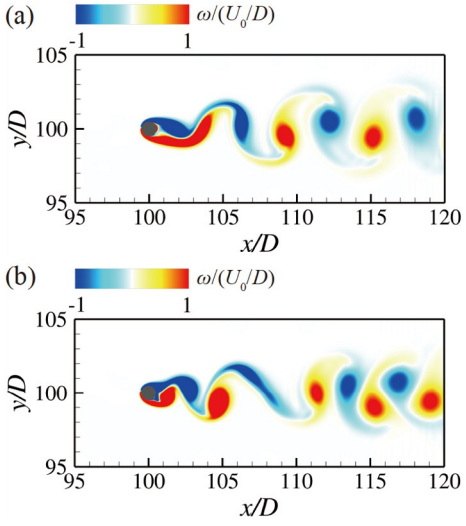

Figure 7 Instantaneous vortex shedding of the oscillating cylinder for (a) $f = 0.15$ and (b) $f = 0.22$.

The spectrums of sound pressure at monitor point $(r, \theta) = (80D, 90°)$ are presented in Fig. 8. When $f = 0.15$, there is only one fundamental frequency, which is equal to the

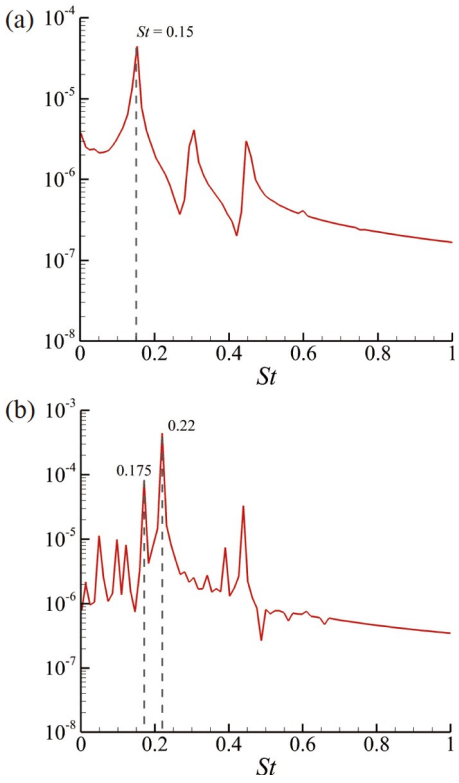

Figure 8 Spectrums of sound pressure at monitor point (80D, 90°) for (a) f = 0.15 and (b) f =0.22.

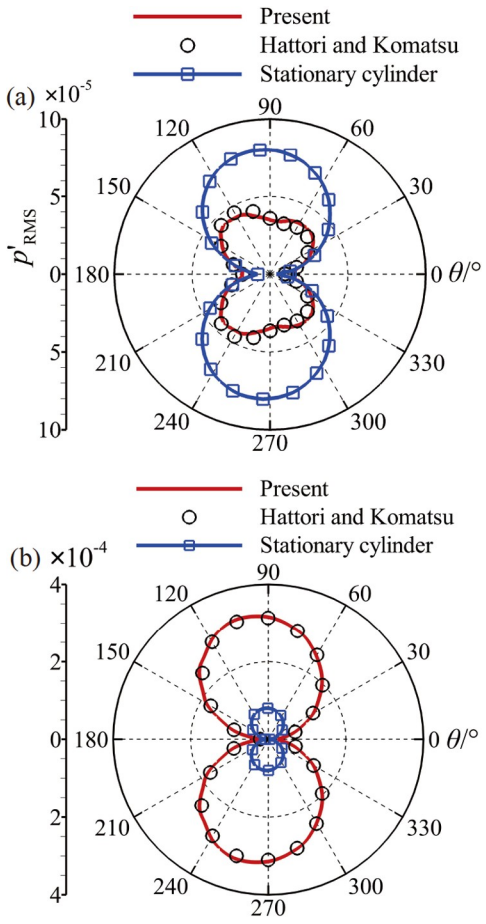

Figure 9 Directivity patterns of sound pressure at r = 80D for (a) f = 0.15 and (b) f =0.22.

motion frequency. The sound field is generated in response to the oscillating motion. However, two fundamental frequencies appear for f = 0.22, which are equal to the oscillation frequency 0.22 and the vortex shedding frequency of the stationary cylinder 0.175, respectively. This implies that the sound field for f = 0.22 is dominated by the oscillatory motion and stationary vortex street. The spectrums of sound pressure are consistent with the flow fields in Fig. 7, where periodic and non-periodic vortex shedding are observed for f = 0.15 and f = 0.22, respectively. The sound pressure directivity patterns at r = 80D are presented in Fig. 9. The stationary cylinder is plotted for comparison. The sound field for f = 0.22 presents a lift dipole source and the radiated sound pressure is higher than that stationary cylinder. However, the directivity pattern for f = 0.15 presents distinct features, and the magnitude of the radiated sound is lower than that f = 0.22 and the stationary cylinder. The present directivity patterns match well with the compressible DNS solutions [17], which validates the accuracy of the present method for large displacement problems.

3.3 Sound generated by flow past oscillating and stationary cylinders

In this case, the flow-induced sound generated by oscillating and stationary cylinders in tandem is simulated to demonstrate the present method for multiple moving bodies with relative motion. Two cases are considered in Fig. 10. The first case is that the motion cylinder is oscillated in front of the stationary cylinder (oscillating-stationary cylinder array) and the second case is that the motion cylinder is oscillated behind the stationary cylinder (stationary-oscillating cylinder array). Two cylinders with diameter D = 1 are arranged in tandem in a uniform flow U_0. The initial distance between the center of two cylinders is 2D and the motion equation of the oscillating cylinder is $y(t) = 0.2\sin(2\pi t \times 0.14)$. The Re = 150 and Ma = 0.2. The computational domain is $0 \le (x, y) \le 200D$ and a non-uniform 704 × 512 grid with a minimum grid of 0.01D is used.

The time histories of the lift coefficients of the two cases are shown in Fig. 11. The amplitudes of the lift fluctuations are different for the two cases. For the oscillating-stationary cylinder array, the amplitudes of lift fluctuations of the oscillating cylinder and the stationary cylinder are close, which are about 0.63 and 0.78, respectively. For the stationary-oscillating cylinder array, the value for the front oscillating cylinder is 0.52, about 2.5 times that for the aft stationary one, 0.21. The instantaneous vorticity fields at the moment of maximum lift coefficient, 0.78 and 0.52, both on the aft cylinder, for the two cases are presented in Fig. 12. It

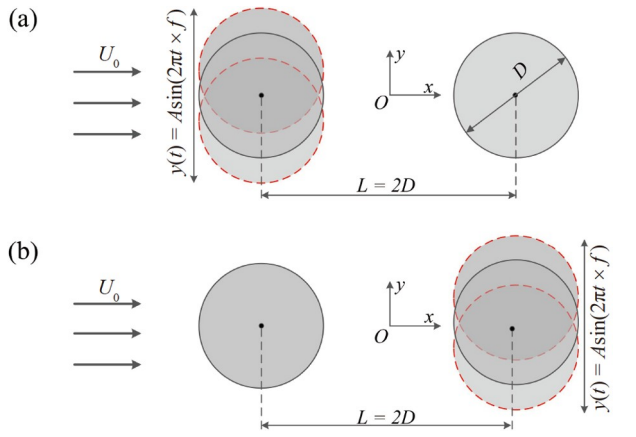

Figure 10 Computational modeling of flow past an oscillating cylinder and a stationary cylinder: (a) oscillating-stationary cylinder array; (b) stationary-oscillating cylinder array.

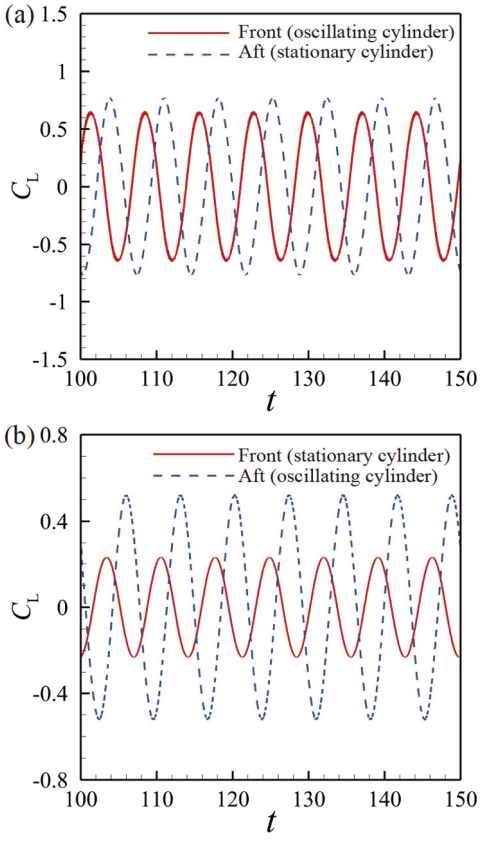

Figure 11 Time histories of lift coefficients for the (a) oscillating-stationary cylinder array and (b) stationary-oscillating cylinder array.

shows that the vortex structures behind the downstream cylinder of the two arrays are similar. However, the vortex structure between the two cylinders is different. For an oscillating-stationary cylinder array, a vortex generated by the upstream cylinder comes into collision with the downstream cylinder on the upper edge, and the lift coefficient of the aft stationary cylinder goes to maximum, 0.78. For a stationary-oscillating cylinder array, a positive vortex is about to be

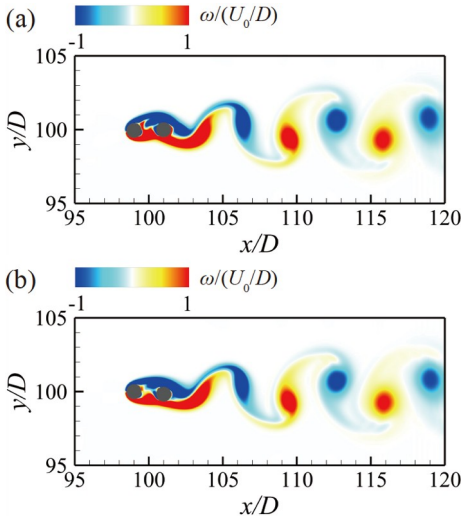

Figure 12 Instantaneous vortex shedding contours for the (a) oscillating-stationary cylinder array and (b) stationary-oscillating cylinder array, at the time when the lift coefficient of the aft cylinder goes to maximum.

shed from the lower side of the stationary cylinder, while another negative vortex is generated on the other side of the oscillating cylinder. At this time the lift coefficient of the aft oscillating cylinder arrives the maximum, 0.52.

The sound fields produced by two cases are presented in Fig. 13. For the stationary-oscillating cylinder array, the sound waves in Fig. 13(b) present a dipolar sound similar to the stationary cylinder. However, the sound field of the oscillating-stationary cylinder array in Fig. 13(a) does not exhibit a dipolar nature. The sound waves at ±45° in the downstream direction are dominant and the sound pressure is weak in the upstream direction. Besides, the wave length in the upstream direction is smaller compared with that in the ±45° direction. The directivity patterns at $r = 80D$ are presented and compared with existing results in Fig. 14. The directivity patterns are similar to the sound fields in Fig. 13 and the magnitude of sound pressure for oscillating-stationary cylinder array is significantly reduced compared with that of the stationary-oscillating cylinder array, which is closely related to the vorticity field and fluid force fluctuation of the cylinder array. The present results, as for vortex motion and sound propagation, match well with the DNS solutions [17], which validates the accuracy of the present method for complicated multiple moving bodies.

As the validation cases of sound wave propagation show, the accuracy of the analytic problem drops from 4 to 2.3 with the boundary involved [23]. For the nonlinear problems, such as most of the flow-induced sound generation cases, the specific accuracy is hard to evaluate. As known, the sound source is strongly related to the gradient or time-derivative of pressure and the sound source might be adjacent to the moving body but the sound speed is much larger than convective velocity for most problems, thus the effect of the numerical treatment would be global, i.e., it

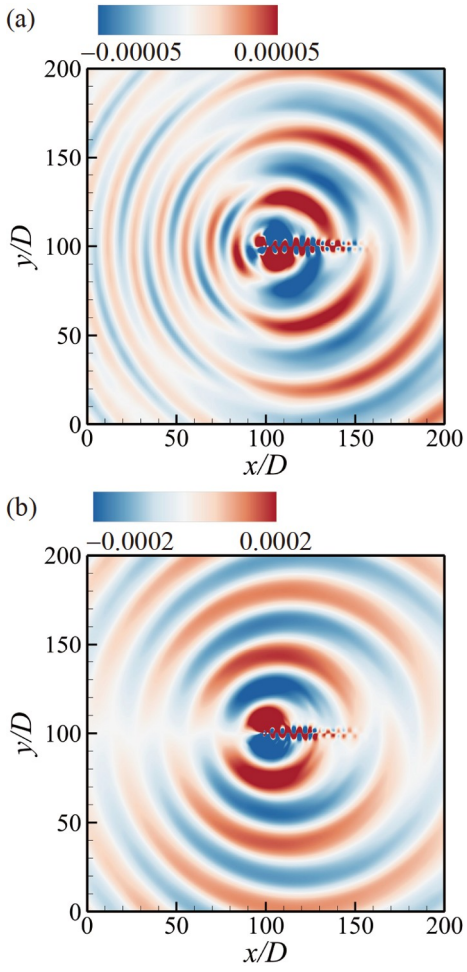

Figure 13 Instantaneous sound fields for the (a) oscillating-stationary cylinder array and (b) stationary-oscillating cylinder array.

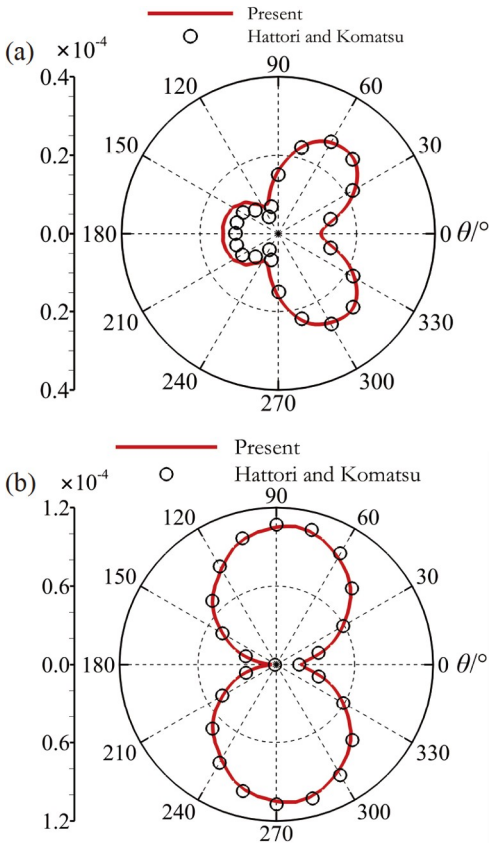

Figure 14 Directivity patterns at $r = 80D$ for the (a) oscillating-stationary cylinder array and (b) stationary-oscillating cylinder array.

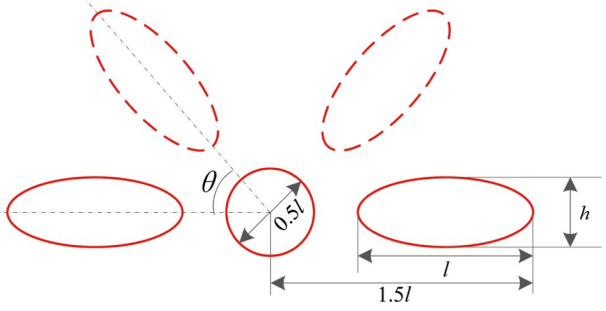

Figure 15 Schematic of the flapping wing model.

would affect the whole domain soon. However, refinement of the grid, especially with the adaptive mesh refinement [34] technique, more accurate results could be obtained, in the near future.

3.4 Sound generated by flapping wings in hovering flight

The sound generated by flapping wings of an insect in its hovering flight is considered a typical application of the present method for bio-inspired locomotion. The schematic of the computational modeling is shown in Fig. 15. The insect body is a stationary cylinder with a diameter $0.5l$ and the flapping wings are represented by two ellipses. The lengths of the major axis (l_{major}) and minor axis (l_{minor}) of the wings are l and h, respectively. The flapping angular velocity $\dot{\theta} = \mathbf{U}_{max}/r_{tip} \sin(2\pi ft)$ [18,35], where $\mathbf{U}_{max}$ is the maximum linear velocity of the wing tip, $r_{tip} = 1.5l$ is the distance between the body center and the wing tip, and f is the flapping frequency. The $Re = \mathbf{U}_{max}l/\nu_0 = 200$, $Ma = \mathbf{U}_{max}/c_0 = 0.1$ and Strouhal number $St = lf/\mathbf{U}_{max} = 0.25$. A Cartesian grid system with 640 × 640 grids is used and the minimum grid size is $0.01l$.

The instantaneous sound field for $h = 0.4l$ is presented in Fig. 16(a). The flapping motion generates a dipole sound source and the wavelength of the sound wave is $40l$, which is very close to the results based on the St and Ma ($= c_0 l/(Ma \cdot St)$). The time histories of sound pressure recorded at the up point $(0, 160l)$ and down point $(0, 40l)$ are compared with results in the Ref. [35] in Fig. 16(b). Good agreements of the results demonstrate the capability of the current method in handling large displacement problems.

In nature, the insect wings have evolved into different shapes for communication, prey, and courtship, not only for

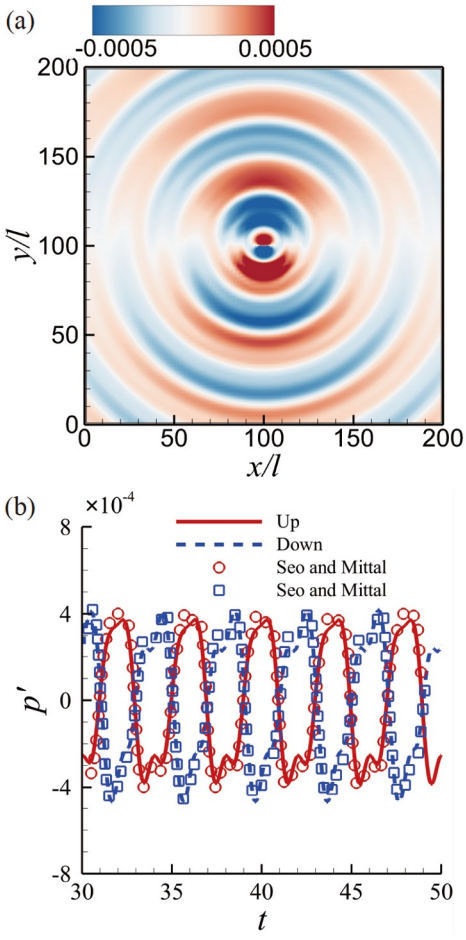

Figure 16 (a) Instantaneous sound field. (b) Time histories of the sound pressure at the up and down monitor points for $h = 0.4l$

the use of lift for flight, but also the sound for mating. For example, the wings of mosquitoes are slenderer than those fruit fly and butterfly, and the buzz generated by the mosquito is annoying to humans, but is important for a male to search and identify the females. In order to investigate the influence of wing shape on the sound field, the aspect ratio AR (= l/h) of the wings is modified by changing the length of the minor axis h. The h are set as $0.2l$, $0.4l$, $0.6l$, and $0.8l$, and the AR are 5.0, 2.5, 1.67, and 1.25, respectively. The directivity patterns for varied aspect ratios at $60l$ are presented in Fig. 17. It shows that all of the directivity patterns of the wing model are dominated by the lift dipole. However, the magnitudes of the sound pressure present different features. The sound pressure is maximum at AR = 5.0, indicating that the slender insect wing (such as a mosquito) facilitates the generation of wing-tones. The sound pressure decreases rapidly and varies slightly with increasing AR. The present results show that the high wing aspect-ratio adopted by insects (such as mosquitoes) can generate high-intensity wing-tones compared to similarly sized insects such as fruit flies and butterflies at a constant wing beat frequency.

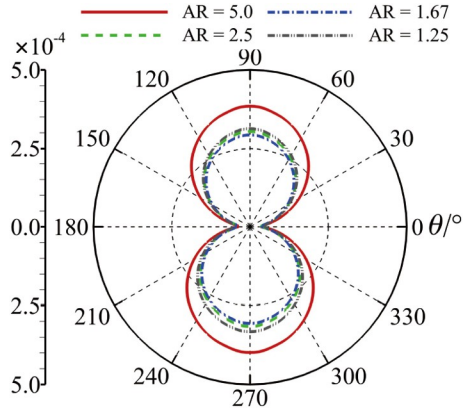

Figure 17 Directivity patterns for varied aspect ratios.

3.5 Sound generated by flow over two undulatory foils in tandem

The last problem is about the sound generation by flow over two undulatory foils in tandem in a uniform flow, which could be a model representing the collective fish propulsion. The fish swimming and school is a mysterious phenomenon, with the other collective locomotion of animal, including swarm of starlings, which has attracted many research works from different points of views [36-38]. The flow physics and the animal acoustics need to be revealed that if the fishes in the school communicate by acoustics [33,39,40]. The simplified locomotion of the two-foil system is a complex problem whereas multiple bodies with large deformations and time-varying geometries are involved. The traveling waveform is applied on each NACA 0012 foil (chord length $L = 1$) to model the locomotion [41]. The instantaneous lateral displacement $y(x, t)$ is described as

$$y(x, t) = a(x)\sin(kx - 2\pi f_0 t + \varphi),\ x \in [0,1], \tag{12}$$

where $k = 2\pi$ is the wave number; f_0 is the frequency; φ is the initial phase. The envelope of the wave $a(x)$ is expressed as

$$a(x) = a_0 + a_1 x + a_2 x^2. \tag{13}$$

The constants a_0, a_1, and a_2 are 0.02, −0.08, and 0.16 respectively to model the carangiform motion of the fish [41]. The midlines of the foil during a tail-beat period are presented in Fig. 18(a). The St (= $2a_{\max} f_0/U_0$) based on the peak-to-peak tail beat amplitude $2a_{\max}$ and f_0 is 0.42 to satisfy the steady-swimming condition [31] in a uniform incoming flow U_0. The $Re = U_0 L/\nu_0$ =1000 and $Ma = U_0/c_0$ = 0.01. The schematic of the foil system is presented in Fig. 18(b) and the longitudinal spacing S between two foils is $1.1L$ to represent the dense foil system. The phases of the upstream and downstream foils are denoted by φ_1 and φ_2, respectively. In this case, φ_1 is set to a constant value of 0° and φ_2 varies from 0° to 360° at intervals of 90°. The computational domain size is $200L \times 200L$ and a non-uniform 1664 × 448 grid with minimum grid spacing $0.005L$ is

applied near the foil.

The vortex structures of the foil system for varied phases are presented in Fig. 19. The vortex shed from the upstream foil collides with the downstream foil and interacts with the vortex shed from the downstream foil. The vortex patterns show different characteristics in the varied phase differences. However, the flow patterns generated by the two foils are similar when it attached and shed in the foils, and the different flow features are mainly determined by the vortex street formed behind the downstream foil and in the wake. Note that the parameters of undulation kinematics, say undulating amplitude and frequency, are chosen to balance the hydrodynamic thrust and drag basically. When $\varphi_2 = 0°$, the two foils undulate synchronously and the vortices behind the downstream foil form a series of remarkable vortex pairs at two sides, which generates a quite wide wake, besides, a series of stronger core vortices are arranged in the centerline of the trail. For $\varphi_2 = 90°$, the strong core vortices remain but the side vortex pairs are weaker, and in the far wake there are two zig-zag vortex pairs remained, which form a reversed von Kármán vortex street. For $\varphi_2 = 180°$ and 270°, the reversed von Kármán vortex street generates behind the foil, and the side vortex pairs seem to disappear due to its weakness, especially for $\varphi_2 = 180°$. Based on the width of the trailing vortices, there exists a sequence of φ_2, arranged from largest to smallest, in the following order, 0°, 90°, 270°, and 180°, among the four cases.

The directivity patterns measured at $r = 60L$ for varied phases are presented in Fig. 20. It shows that all acoustic directivities present a dipolar sound source pattern in line with expectations, which has been observed in the situation for a single-foil and foil system in side-by-side arrangement. When $\varphi_2 = 0°$, 90°, and 270°, the intensity in the vertical direction (lift-dipole) is higher than that in the horizontal direction (drag-dipole) and the sound fields are dominated by the lift dipole. The magnitude of the sound pressure at 0° phase is slightly higher than that at 90° phase and both are higher than that at 270° phase. When $\varphi_2 = 180°$, two foils perform the anti-phase motion, the lift dipole (vertical direction) decreases and the drag dipole (horizontal direction) increases, and the directivity pattern is nearly elliptical, more like a stretched monopole. The magnitude relation among the four situations is accordant with the flow feature, as analyzed in the above paragraph. It is worth noticing that the sound pressure decreases significantly due to the destructive interference of the sound. The instantaneous sound fields of the two foils for $\varphi_2 = 0°$ and $\varphi_2 = 180°$ are further presented in Fig. 21. The difference of the two sound fields is significant. The results demonstrate the versatility of the solver for moving bodies with large deformations and show the potential of the approach for simulating sound generated by bio-inspired motions.

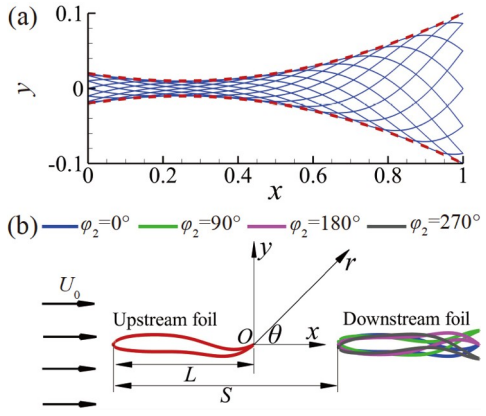

Figure 18 (a) The midlines of the foil during a motion period and the dashed line is the amplitude of the traveling wave. (b) Model of the tandem foil system with varied phases.

4. Conclusions

In the present study, we develop a versatile DNS-APE hybrid approach based on the IBM for simulating flow-in-

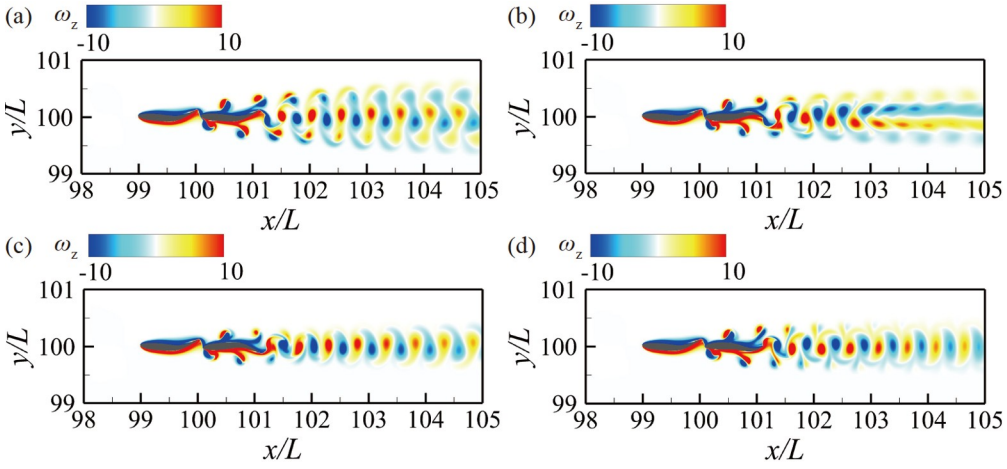

Figure 19 Instantaneous vortex shedding of the tandem foil for varied phases φ_2 ($\varphi_1 = 0°$). (a) $\varphi_2 = 0°$; (b) $\varphi_2 = 90°$; (c) $\varphi_2 = 180°$; (d) $\varphi_2 = 270°$.

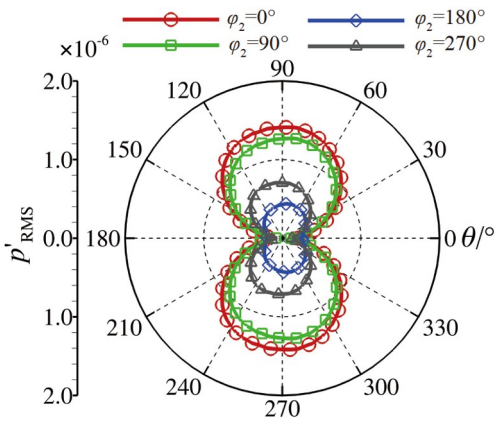

Figure 20 Directivity patterns measured at $r = 60L$ at varied phases.

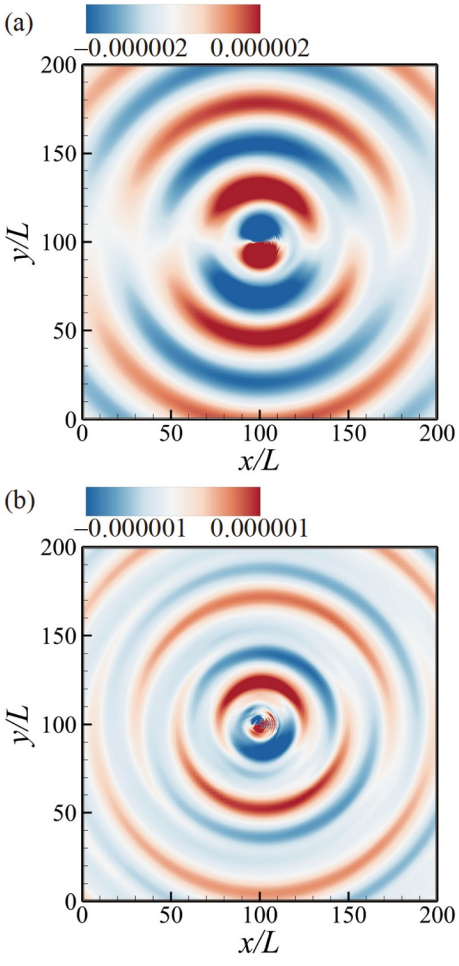

Figure 21 Sound fields of the two foils for (a) $\varphi_2 = 0°$ and (b) $\varphi_2 = 180°$.

duced sound problems involving complex moving boundaries. Our approach involves simulating the incompressible flow field using a second-order DNS flow solver and predicting the sound field by solving APE, the acoustic propagation equation. We employ a GC based IBM for both the flow solver and the acoustic solver. This method is suitable for simulations involving large displacements and deformations with high accuracy, while maintaining sharp interface properties. We validate the accuracy and fidelity of our DNS-APE hybrid method for moving boundaries by simulating sound generated by the flow past cylinders undergoing different motions, including translation and rotation, as well as their combinations. Furthermore, we explore the sound generated by the flapping wings in hovering insect flight and the undulatory swimming of tandem fish-like foils, as representative bio-inspired applications. Our results provide new insights into challenging bio-fluid flow and bio-acoustics with complex solid boundaries and complex motions, especially overcoming the limits of acoustic analogy methods in portraying complicated acoustic phenomena, such as scattering, reflecting, etc. These demonstrations underscore the potential of the DNS-APE method and immersed boundary treatment for dealing with moving bodies, making it applicable to practical scenarios involving bio-fluids, bio-inspired aerial/underwater vehicles, and rotating machinery.

Conflict of interest *On behalf of all authors, the corresponding author states that there is no conflict of interest.*

Author contributions *Cheng Zhao and Yan Yang designed the research. Yan Yang supervised and administrated the investigations. Cheng Zhao developed the original code of APE solver, performed the data post-process. Cheng Zhao and Yan Yang performed data analysis and wrote the first draft of the manuscript. Hong-Gang Li, Xue-Gang Li, and Kai Cui helped organize the manuscript. Yan Yang and Cheng Zhao revised and edited the final version. Hong-Gang Li, Xue-Gang Li, and Kai Cui helped on computational resources.*

Acknowledgements *This work was supported by the National Natural Science Foundation of China (Grant Nos. 52301380 and 11602277). Cheng Zhao and Yan Yang appreciate Prof. Haibo Dong's help on the CFD solver during their visit. Authors thank the anonymous referees' helpful suggestions which improved the quality of the paper.*

1 F. E. Fish, Advantages of aquatic animals as models for bio-inspired drones over present AUV technology, Bioinspir. Biomim. **15**, 025001 (2020).
2 X. He, Y. Liu, Y. Chen, and S. Wang, Wake of a bio-inspired flapping wing with morphing wingspan, Acta Mech. Sin. **39**, 323061 (2023).
3 M. Marcin, S. Adam, Z. Jerzy, and M. Marcin, Fish-like shaped robot for underwater surveillance and reconnaissance—Hull design and study of drag and noise, Ocean Eng. **217**, 107889 (2020).
4 J. H. Seo, T. L. Hedrick, and R. Mittal, Mosquitoes buzz and fruit flies don't-a comparative aeroacoustic analysis of wing-tone generation, Bioinspir. Biomim. **16**, 046019 (2021).
5 M. Short, P. R. White, T. G. Leighton, and P. S. Kemp, Influence of acoustics on the collective behaviour of a shoaling freshwater fish, Freshwater Biol. **65**, 2186 (2020).
6 A. N. Popper, and J. A. Sisneros, The sound world of zebrafish: A critical review of hearing assessment, Zebrafish **19**, 37 (2022).
7 M. Wang, J. B. Freund, and S. K. Lele, Computational prediction of flow-generated sound, Annu. Rev. Fluid Mech. **38**, 483 (2006).
8 S. Schoder, and M. Kaltenbacher, Hybrid aeroacoustic computations: State of art and new achievements, J. Theor. Comp. Acout. **27**, 1950020 (2019).
9 J. C. Hardin, and D. S. Pope, An acoustic/viscous splitting technique for computational aeroacoustics, Theoret. Comput. Fluid Dyn. **6**, 323 (1994).

10 W. Z. Shen, J. A. Michelsen, and J. N. Sørensen, A collocated grid finite volume method for aeroacoustic computations of low-speed flows, J. Comput. Phys. **196**, 348 (2004).
11 W. Z. Shen, and J. N. Sørensen, Aeroacoustic modelling of low-speed flows, Theor. Comput. Fluid Dyn. **13**, 271 (1999).
12 R. Ewert, and W. Schröder, Acoustic perturbation equations based on flow decomposition *via* source filtering, J. Comput. Phys. **188**, 365 (2003).
13 J. H. Seo, and Y. J. Moon, Linearized perturbed compressible equations for low Mach number aeroacoustics, J. Comput. Phys. **218**, 702 (2006).
14 C. S. Peskin, Flow patterns around heart valves: A numerical method, J. Comput. Phys. **10**, 252 (1972).
15 R. Mittal, and G. Iaccarino, Immersed boundary methods, Annu. Rev. Fluid Mech. **37**, 239 (2005).
16 R. Komatsu, W. Iwakami, and Y. Hattori, Direct numerical simulation of aeroacoustic sound by volume penalization method, Comput. Fluids **130**, 24 (2016).
17 Y. Hattori, and R. Komatsu, Mechanism of aeroacoustic sound generation and reduction in a flow past oscillating and fixed cylinders, J. Fluid Mech. **832**, 241 (2017).
18 L. Wang, F. B. Tian, and J. C. S. Lai, An immersed boundary method for fluid-structure-acoustics interactions involving large deformations and complex geometries, J. Fluids Struct. **95**, 102993 (2020).
19 L. Cheng, L. Du, X. Wang, X. Sun, and P. G. Tucker, A semi-implicit immersed boundary method for simulating viscous flow-induced sound with moving boundaries, Comput. Methods Appl. Mech. Eng. **373**, 113438 (2021).
20 J. H. Seo, and R. Mittal, A high-order immersed boundary method for acoustic wave scattering and low-Mach number flow-induced sound in complex geometries, J. Comput. Phys. **230**, 1000 (2011).
21 F. Xie, Y. Qu, M. A. Islam, and G. Meng, A sharp-interface Cartesian grid method for time-domain acoustic scattering from complex geometries, Comput. Fluids **202**, 104498 (2020).
22 Y. He, X. Zhang, T. Zhang, J. Geng, J. Liu, and X. Chen, An improved hydrodynamic/acoustic splitting method for fluid-structure interaction feedback with elastic boundaries, Phys. Fluids **34**, 023606 (2022).
23 C. Zhao, Y. Yang, T. Zhang, H. Dong, and G. Hou, A sharp interface immersed boundary method for flow-induced noise prediction using acoustic perturbation equations, Comput. Fluids **227**, 105032 (2021).
24 R. Mittal, H. Dong, M. Bozkurttas, F. M. Najjar, A. Vargas, and A. von Loebbecke, A versatile sharp interface immersed boundary method for incompressible flows with complex boundaries, J. Comput. Phys. **227**, 4825 (2008).
25 C. K. W. Tam, and J. C. Webb, Dispersion-relation-preserving finite difference schemes for computational acoustics, J. Comput. Phys. **107**, 262 (1993).
26 C. K. W. Tam, Computational aeroacoustics-Issues and methods, AIAA J. **33**, 1788 (1995).
27 F. Q. Hu, M. Y. Hussaini, and J. L. Manthey, Low-dissipation and low-dispersion Runge-Kutta schemes for computational acoustics, J. Comput. Phys. **124**, 177 (1996).
28 C. Bogey, and C. Bailly, A family of low dispersive and low dissipative explicit schemes for flow and noise computations, J. Comput. Phys. **194**, 194 (2004).
29 C. K. W. Tam, and Z. Dong, Radiation and outflow boundary conditions for direct computation of acoustic and flow disturbances in a nonuniform mean flow, J. Comp. Acous. **04**, 175 (1996).
30 C. Zhao, T. Zhang, and G. X. Hou, Finite-difference time-domain modeling for underwater acoustic scattering applications based on immersed boundary method, Appl. Acoustics **193**, 108764 (2022).
31 C. Zhao, T. Zhang, Y. Yang, and H. Dong, Sound generated by flow over two traveling wavy foils in a side-by-side arrangement, Phys. Fluids **34**, 127120 (2022).
32 O. Inoue, M. Mori, and N. Hatakeyama, Control of aeolian tones radiated from a circular cylinder in a uniform flow, Phys. Fluids **15**, 1424 (2003).
33 M. S. U. Khalid, I. Akhtar, and B. Wu, Quantification of flow noise produced by an oscillating hydrofoil, Ocean Eng. **171**, 377 (2019).
34 W. Zhang, Y. Pan, J. Wang, V. Di Santo, G. V. Lauder, and H. Dong, An efficient tree-topological local mesh refinement on Cartesian grids for multiple moving objects in incompressible flow, J. Comput. Phys. **479**, 111983 (2023).
35 J. H. Seo, R. Mittal, in Computation of aerodynamic sound around complex stationary and moving bodies: Proceedings of the 49th AIAA Aerospace Sciences Meeting including the New Horizons Forum and Aerospace Exposition, Orlando, 2011, p. 1087.
36 W. Sun, G. He, F. Jin, Q. Wang, and F. Yu, Numerical study and parameter prediction of a full-free flexible flament in wakes of flapping wing, Acta Mech. Sin. **40**, 323247 (2024).
37 X. T. Huang, P. N. Sun, H. G. Lyu, and S. Y. Zhong, Study of 3D self-propulsive fish swimming using the δ+-SPH model, Acta Mech. Sin. **39**, 722053 (2023).
38 L. Liu, G. He, X. He, Q. Wang, and L. Chen, Numerical study on the effects of a semi-free and non-uniform flexible filament in different vortex streets, Acta Mech. Sin. **37**, 929 (2021).
39 N. Wagenhoffer, K. W. Moored, and J. W. Jaworski, Unsteady propulsion and the acoustic signature of undulatory swimmers in and out of ground effect, Phys. Rev. Fluids **6**, 033101 (2021).
40 N. Wagenhoffer, K. W. Moored, and J. W. Jaworski, On the noise generation and unsteady performance of combined heaving and pitching foils, Bioinspir. Biomim. **18**, 046011 (2023).
41 A. Gilmanov, and F. Sotiropoulos, A hybrid Cartesian/immersed boundary method for simulating flows with 3D, geometrically complex, moving bodies, J. Comput. Phys. **207**, 457 (2005).

基于虚拟网格浸入边界法的运动物体流噪声混合模拟方法

赵成, 李红钢, 黎雪刚, 杨焱, 崔凯

摘要 发展了基于浸入边界法的流噪声混合模拟方法, 用于模拟运动体引起的流噪声. 不可压流动采用高保真直接数值模拟(DNS)求解器; 声传播方程(APE)用于模拟声场. 其中后者采用色散关系保持空间格式和低色散低耗散龙格库塔时间格式. 该DNS-APE两步法将基于虚拟单元的锐利界面浸入边界法应用在笛卡尔网格上处理复杂运动边界. 验证算例包括旋转单圆柱、振荡单圆柱以及串联静止和振荡圆柱组合所产生的流噪声. 研究了不同形状扑翼飞行运动和串联集群波状游动两种典型复杂仿生运动所产生的声场. 本文展示了该高精度混合方法在模拟具有复杂运动边界的流动诱发的噪声产生和传播(声场)方面具备有效性, 尤其是在预测生物或仿生机器所产生的流动噪声特性方面, 可为动物声学、动物复杂系统行为学和相关仿生工程的低噪声设计等方面的研究和开发提供相关理论依据和概念.